



**University of Dundee**

## **On bore dynamics and pressure**

Liu, Jiaqi; Hayatdavoodi, Masoud; Ertekin, R. Cengiz

*Published in:*  
Journal of Offshore Mechanics and Arctic Engineering

*DOI:*  
[10.1115/1.4044988](https://doi.org/10.1115/1.4044988)

*Publication date:*  
2020

*Document Version*  
Peer reviewed version

[Link to publication in Discovery Research Portal](#)

*Citation for published version (APA):*  
Liu, J., Hayatdavoodi, M., & Ertekin, R. C. (2020). On bore dynamics and pressure: RANS, GN, and SV Equations. *Journal of Offshore Mechanics and Arctic Engineering*, 142(2), Article 021902.  
<https://doi.org/10.1115/1.4044988>

### **General rights**

Copyright and moral rights for the publications made accessible in Discovery Research Portal are retained by the authors and/or other copyright owners and it is a condition of accessing publications that users recognise and abide by the legal requirements associated with these rights.

### **Take down policy**

If you believe that this document breaches copyright please contact us providing details, and we will remove access to the work immediately and investigate your claim.

# On bore dynamics and pressure: RANS, GN, and SV Equations

Jiaqi Liu

Civil Engineering Department  
University of Dundee  
Dundee, DD1 4HN, UK  
Email: j.o.liu@dundee.ac.uk

Masoud Hayatdavoodi \*

Civil Engineering Department  
University of Dundee  
Dundee, DD1 4HN, UK  
Email: mhayatdavoodi@dundee.ac.uk

R. Cengiz Ertekin †

Ocean and Resources Engineering Department  
SOEST, University of Hawaii at Manoa  
2540 Dole St., Holmes 402, Honolulu, HI 96822  
Email: erteekin@hawaii.edu

*Propagation and impact of two and three dimensional bores generated by breaking of a water reservoir is studied by use of three theoretical models. These include the Reynolds-Averaged Navier-Stokes (RANS) equations, the Level I Green-Naghdi (GN) equations and the Saint-Venant (SV) equations. Two types of bore generations are considered, namely (i) bore generated by dam-break, where the reservoir water depth is substantially larger than the downstream water depth, and (ii) bore generated by an initial mound of water, where the reservoir water depth is larger but comparable to the downstream water depth. Each of these conditions correspond to different natural phenomena. This study show that the relative water depth play a significant role on the bore shape, stability and impact. Particular attention is given to the bore pressure on horizontal and vertical surfaces. Effect of fluid viscosity is studied by use of different turbulence closure models. Both two and three dimensional computations are performed to study their effect on bore dynamics. Results of the theoretical models are compared with each other, and with availably laboratory experiments. Information is provided on bore kinematics and dynamics predicted by each of these models. Discussion is given on the assumptions made by each model and differences in their results. In summary, SV equations have substantially simplified the physics of the problem, while results of the GN equations compare well with the RANS equations, with incomparable computational cost. RANS equations provide further details about the physics of the problem.*

**Keywords:** Dam break, initial mound of water, Reynolds-Averaged Navier-Stokes equations, Green-Naghdi equations, Saint Venant equations

## 1 Introduction

Bore is generated due to the collapse of a block of fluid. The block of fluid maybe initially at rest (in the case of bores generated by collapse of a reservoir) or in the form of a stable moving wave (in the case of bores generated by solitary wave breaking) [1–3]. Many studies have focused on the bore impact on (a) the downstream wall at the end of tank [2, 4–9] (b) structures in the middle of the tank [10–13] and (c) the upstream wall and side walls [14–19]. Few works have been carried out to study the dynamics of bore. Bore dynamics depend on the generation mechanisms and the downstream conditions. Dam-break and initial mound of water are two examples of bore generation due to a reservoir. The difference between these two cases is the level of the downstream water depth, which results in different bore behaviours.

Propagation of water surging over dry or wet beds is studied as dam-break problems. Examples of dam-break problems are the flash flood caused by dam failure, debris flow surges and tsunami bore runoff on a dry land. Due to the large inertia and impact of the sudden interaction of the body of fluid with structure in a dam-break, immense damages may occur.

There are many examples of the vast damages made by dam-break impact. On December 1, 1923, one buttress of the Gleno Dam in Italy was destroyed and about  $4500000m^3$  of water rushed out from the reservoir behind the dam from an elevation of about  $1535m$  above the sea level to the valley below. 356 lives were lost in this disaster, see [20]. On June 5, 1976, due to the piping and internal erosion at the foot of the Teton Dam in the United States, the right-bank of the main dam wall disintegrated. At a flow rate of  $57000m^3/s$ , muddy water run off the reservoir into the Teton River canyon. The damage was estimated at 2 billion USD and 11 people died in this disaster, see [21]. Due to the epicentre off the west

\*Address all correspondence to M. Hayatdavoodi (MHayatdavoodi@dundee.ac.uk).

†Fellow, ASME

coast of Sumatra, Indonesia, on 26 December 2004, a series of devastating tsunamis, with a height of about 30m, arrived at coastal communities, see [22]. With about 250000 killed in 14 countries, the tsunami is recorded as one of the deadliest natural disasters in the history, see [23] for further details.

Perhaps one of the first studies on dam break flows is that of [24], who introduced theoretical solution of dam break flows based on the shallow water theory. More recently, numerous studies on dam break flows have been carried out, but the dynamics of dam break flows have not been thoroughly studied before 1999. The constrained interpolation profile (CIP) method is adopted by [25] for their CFD model to study the pressure on the downstream wall of a dam-break case. The numerical simulation results of pressure are compared with experiments. Good agreement is achieved by their CIP-based method. [26] present a series of numerical results of dam-break pressure, based on Glimm's method. [27] studied the problem by use of volume of fluid method to determine the pressure closer to the horizontal bed. [28] carried out a similar study but their simulations are focused on examining sloshing physics. Dam-break experiments are carried out by [29] to study the bore propagation and magnitude of the pressure on the downstream wall. More works are required to understand the bore propagation and impact.

Another form of bore generation is due to the breaking of an initial mound of water. The fundamental difference between dam-break and initial mound of water is due to the ratio of the reservoir depth to the downstream water depth. In the dam-break problems, this ratio is larger than 2 (approximately) while this ratio is smaller than 2 for the initial mound of water. This difference in downstream water depth results in different form of flow generation.

Shown by [30], solitons, a train of solitary waves, are generated by the breaking of an initial mound of water. The first description of solitary wave is given by [31]. After that, many [32–35], have studied solitary wave. [36] provides an exact integral equation to evaluate some properties of the solitary wave, including pressure on the seafloor. [37, 38] provide pressure functions derived from linear wave theory which is not suitable for nonlinear waves, including solitary waves. In the theory given by [39], the pressure variation over the water column of solitary wave is linear.

In this work, we will study both types of bores, generated by a dam-break and by an initial mound of water. Although many works have focused on estimating the bore pressure distribution, the descriptions of that of bore on the downstream wall and floor are still not very clear. It is important to find an appropriate model which can calculate the bore pressure correctly, both for engineering and scientific applications. Our goal in this work is to study the bore pressure of a dam break and initial mound of water on vertical and horizontal surfaces, using both linear-based and nonlinear approaches.

This study is concerned with the calculation of bore generation and pressure on the horizontal floor and vertical walls. Three theoretical approaches are used to study this problem, including the Reynolds-Averaged Navier-Stokes

equations, the Green-Naghdi equations and the Saint Venant equations. Our goal is to determine whether these models can provide acceptable results of the bore propagation and pressure, and to provide discussion on their limitations and restrictions. The models are discussed first, followed by results for the dam-break and initial mound of water.

## 2 The Theories

Three sets of equations are used in this study, namely the Reynolds-Averaged Navier-Stokes (RANS) equations, the Green-Naghdi (GN) equations and the Saint Venant (SV) equations. These are discussed in this section. We adopt a right-handed three dimensional (3D) Cartesian coordinate system, with  $x_1$  pointing to the right,  $x_2$  pointing vertically opposite to the direction of the gravitational acceleration ( $x_2 = 0$  corresponds to the sea-floor), and  $x_3$  pointing into the paper. Indicical notation and Einstein's summation convention are used. Subscripts after comma indicate differentiation.

### Reynolds-Averaged Navier-Stokes Equations

For a homogeneous, Newtonian and incompressible fluid, the three dimensional RANS equations are given by the following conservation of mass and momentum equations:

$$\bar{u}_{i,i} = 0, \quad i = 1, 2, 3 \quad (1)$$

$$\bar{u}_{j,t} + (\bar{u}_i \bar{u}_j + \overline{u'_i u'_j})_{,i} = g_j - \frac{1}{\rho} \bar{p}_{,j} + \nu \bar{u}_{j,ii}, \quad i, j = 1, 2, 3 \quad (2)$$

where  $\bar{f}(x_1, x_2, x_3, t)$  is the time-averaged value of the fluctuating variable,  $\vec{u} = u_i \vec{e}_i$  is the velocity vector, and  $\vec{e}_i$  is the unit normal vector in the  $i$  direction.  $\rho$  is the density of fluid,  $\nu$  is kinematic viscosity,  $\vec{g} = (0, -g, 0)$  is the gravitational acceleration and  $p$  is the pressure.

There are two commonly used turbulence models for the RANS equations, namely, the  $k - \omega$  model and the  $k - \epsilon$  model. [40] have discussed that dissipation is needed in equilibrium turbulent flows, *i.e.*, whose rates of producing and destruction are in near balance. For the energy equation, the relation between the dissipation,  $\epsilon$ , and the turbulent kinetic energy,  $k$ , and length scale,  $L$ , can be written as

$$\epsilon \approx \frac{k^{\frac{3}{2}}}{L}. \quad (3)$$

Substituting  $\epsilon$  into the momentum equation, Eq. (2) gives

$$(\rho \epsilon)_{,t} + (\rho u_j \epsilon)_{,x_j} = C_{\epsilon 1} P_k \epsilon_{,k} - \rho C_{\epsilon 2} \epsilon^{\frac{2}{k}} + (\mu_{t,\sigma_\epsilon} \epsilon_{,x_j})_{,x_j}, \quad (4)$$

where the eddy viscosity  $\mu_t = \rho C_\mu \sqrt{k} L = \rho C_\mu \frac{k^2}{\varepsilon}$ , and the five parameters usually are given as:  $C_\mu = 0.09$ ,  $C_{\varepsilon 1} = 1.44$ ,  $C_{\varepsilon 2} = 1.92$ ,  $\sigma_k = 1.0$  and  $\sigma_\varepsilon = 1.3$ , see [40]. The model based on Eqs. (3) and (4) is called  $k - \varepsilon$  model.

In the  $k - \omega$  model, the kinematic viscosity is related to the turbulent kinetic energy and dissipation. [41] introduced the relation as

$$v_t = \frac{\omega}{\rho k}, \quad (5)$$

where  $v_t$  is the eddy-viscosity,  $k$  is the thermal conductivity and  $\omega$  is the specific turbulence dissipation rate. The value of  $\omega$  is related to the turbulence kinetic energy and turbulence dissipation rate, see [41] and [42] for more details about the  $k - \omega$  model used here.

There are two advantages of using the  $k - \omega$  model for the bore impact problems: the model is applicable to variable pressure gradients, and it is more sensitive to free surface problems, see *e.g.* [43] for discussions. The pressure on the downstream wall is sensitive to the shape of the bore, see [44].

Volume of Fluid method (VOF method), originally introduced by [45], is used to determine the free surface between air and water. A scale function is used to represent the volume of fluid in each cell, see [45].

OpenFOAM is used for the computations of the RANS equations. Boundary conditions used in this study are presented in Table 1. Details of these boundary conditions can be found in *e.g.* [46] and [47].

### The Green-Naghdi Equations

The GN equations are originally obtained by use of the directed fluid sheets theory introduced by [48], and [49]. They are applicable to unsteady, nonlinear flows of inviscid and incompressible fluids. The GN equations satisfy the nonlinear boundary conditions exactly, and postulate the integral balance laws. [50] showed that the GN equation can be obtained from the exact 3D governing equations of an incompressible and inviscid fluid by making a single assumption about the distribution of the vertical velocity along the fluid sheet. The resulting equations satisfy exactly the nonlinear boundary conditions, the mass conservation, and the integrated momentum and moment of momentum, see *e.g.* [51] for details. The GN equations are classified based on their levels, corresponding to the function used for the distribution of the vertical velocity along the water column. In this study, we use the Level I GN equations (or the original GN equations). A linear distribution of vertical velocity is assumed in the Level I equations.

The GN equations are used here in two dimensions and in the form first given by [51]:

$$\zeta_{,t} + [(h + \zeta - \alpha)u_{1,1}] = 0, \quad (6)$$

$$\begin{aligned} \dot{u}_1 + g\zeta_{,1} + \frac{\dot{p}_{,1}}{\rho} = & -\frac{1}{6}[(2\zeta + \alpha)_{,1}\ddot{\alpha} \\ & + (4\zeta - \alpha)_{,1}\ddot{\zeta} \\ & - (h + \zeta - \alpha)(\ddot{\alpha} + 2\ddot{\zeta})_{,1}], \end{aligned} \quad (7)$$

where  $h$  is the water depth.  $\zeta$  is the free surface elevation measured from the still water level (SWL),  $\alpha$  is the elevation of the bottom surface, and  $\hat{p}$  is the pressure on the top surface of the fluid sheet. The superposed dot denotes the material time derivative, and double dot is the second order material derivation.

The GN equations have been applied to many problems of unsteady flow impact on structures, see *e.g.* [52–55] for wave scattering and impact on horizontal surfaces, and [56] and [57] for wave diffraction and impact on vertical surfaces.

Information about high-level GN equations can be found in *e.g.* [30, 58–60]

The GN equations (6) and (7), in the form used here, are only applicable to single phase fluids with continuous top and bottom surfaces. Hence, the GN equations are not applicable to the dam-break cases where wave breaking and air entrapment may occur. The GN equations are only used for the initial mound of water cases.

### Saint-Venant Equations

The SV equations, whose 3D form is called Shallow Water equations, are derived from Eqs. (1) and (2) with three assumptions: (i) the viscous terms are negligible, (ii) pressure is only hydrostatic, and (iii) the fluid flows in one dimension only ( $x_1$  direction), where  $u_2$  is small enough to be omitted, and  $u_1$  is assumed to be constant in  $x_2$ -direction. In the absence of viscous terms, the effect of viscosity is approximated by use of empirical terms and the body force. Hence the SV equations read as, (see [61] and [62]),

$$u_{1,t} + u_1 u_{1,1} = -gh_{,1} + gS - gS_f, \quad (8)$$

where  $S(x_1) = -\alpha_{,x_1}$  is the bed slope,  $S_f(x_1, t) = \frac{\tau}{\rho g R}$  is the friction slope,  $\tau(x_1, t)$  is the shear stress along the wetted perimeter  $p_w(x_1, t)$  at location  $x_1$  and  $R(x_1, t) = \frac{A}{p_w}$  is the hydraulic radius, where  $A(x_1, t)$  is the cross-sectional area of the flow. The shear stress is given by Manning's equation, see [63].

To determine the pressure, we use the unsteady Bernoulli equation. For small-amplitude oscillations, the unsteady Bernoulli equation is given by (see *e.g.* [64]):

$$\phi_{,t} + \frac{p}{\rho} + gx_2 = C, \quad (9)$$

Table 1: Boundary conditions used in the RANS model. For definition of the boundary conditions, see *e.g.* [46] and [47].

Boundary	$\beta$	$p$	$\mathbf{u}$
bottom	zeroGradient	zeroGradient	fixedValue (0,0,0)
front and back walls	zeroGradient	zeroGradient	fixedValue (0,0,0)
upstream and downstream walls	empty	empty	empty
atmosphere	inletOutlet	totalPressure	pressureInletOutletVelocity

where  $\phi$  is the velocity potential,  $C$  is a constant and  $p$  is the pressure. By substituting  $d\phi = u_1 dx_1 + u_2 dx_2$  in Eq. (9), by definition, we obtain

$$\left( \int u_1 dx_1 + \int u_2 dx_2 \right)_t + \frac{p}{\rho} + gx_2 = C, \quad (10)$$

and hence the pressure is determined by:

$$p(x_1, x_2, t) = - \left( \rho gx_2 + \rho \left( \int u_1 dx_1 + \int u_2 dx_2 \right)_t \right). \quad (11)$$

### 3 Numerical Solutions

The three governing equations are solved numerically using various techniques. These are introduced here.

The RANS equations are solved by use of a finite-volume approach. The integral form of the RANS equations, Eqs. (1) and (2) over time and space can be written as:

$$\begin{aligned} & \int_t^{t+\Delta t} \left[ \iint \bar{u}_{j,t} dx_i dx_j + \iint (\bar{u}_i \bar{u}_j + \overline{u'_i u'_j})_i dx_i dx_j \right] dt \\ &= \int_t^{t+\Delta t} \left[ \iint g_j dx_i dx_j \right. \\ & \quad \left. - \iint \frac{1}{\rho} \bar{p}_{,j} dx_i dx_j \right. \\ & \quad \left. + \iint \nu \bar{u}_{j,ii} dx_i dx_j \right] dt, (i, j = 1, 2, 3), \end{aligned} \quad (12)$$

see *e.g.* [65] for more information.

To solve the pressure-velocity coupling in Eq. (12), there are three commonly used algorithms that can be employed, namely the Pressure Implicit Splitting Operator (PISO) algorithm, the Semi-Implicit Method for Pressure-Linked equations (SIMPLE) algorithm and the PISO-SIMPLE (PIMPLE) algorithm. In PIMPLE algorithm, the SIMPLE algorithm is employed to iteratively calculate pressure from velocity component in the Navier-Stokes (RANS) equations and the PISO algorithm is employed to revise the results, see [66] and [40]. The PIMPLE algorithm is often computationally more efficient because a larger Courant number can be used. PIMPLE do not show too much ad-

vantages in simple cases and flow patterns. For more complicated geometries, skewed, non-orthogonal meshes, PIMPLE can stabilize the simulations whereas the case may fail or cost more computational effort with PISO and SIMPLE, see [67].

For the RANS model, the free surface is determined by use of the volume of fluid method. The computations are carried out using an open source computational software, namely OpenFOAM.

The GN equations are solved by use of a central difference scheme, second order in space, and by use of modified Euler's method for time marching. See [51] and [68] for discussion on the solution of the Level I the GN equations as used here. In the GN equations, the function  $\zeta$  (surface elevation) is single-valued. Hence, the GN equations are not applicable to the cases with wave breaking, such as the dam-breaking cases and cases with dry downstream.

The SV equations are solved by use of a finite volume method. The integral form of Eq. (8) over time and space can be written as:

$$\begin{aligned} & \int_t^{t+\Delta t} \int u_{1,t} dx_1 + \int u_1 \partial u_{1,1} dx_1 \Big|_t^{t+\Delta t} = \int_t^{t+\Delta t} \left[ \int -gh_{,1} dx_1 \right. \\ & \quad \left. + \int gS - gS_f dx_1 \right] dt. \end{aligned} \quad (13)$$

Details of the computational model of the SV equations as used here can be found in [69].

### 4 Numerical Setup

Results are given in dimensionless form using  $\rho$ ,  $g$  and  $H$  or  $h$  as a dimensionally independent set. For the dam-break problems,  $p' = p/\rho g H$  and  $t' = t\sqrt{g/H}$ , where  $H$  is the initial dam height, shown in Fig. 1. For the initial mound of water problem,  $p' = p/\rho gh$  and  $t' = t\sqrt{g/h}$ , where  $h$  is the downstream water level.

A grid convergence study is performed to determine the appropriate grid for the computations. Here, we only present the grid convergence of the RANS equations. The convergence test of the GN and the SV equations can be found in *e.g.* [30] and [69], respectively. For the grid convergence study of the RANS model, we consider the experiment of [29].

In the experiments of [29], a tank 1,610mm long, 600mm high and 150mm wide is used. The reservoir is on

Table 2: Grid information of the convergence tests of the 2D RANS equations.

Grid ID	$\Delta x_1/h$	$\Delta x_2/h$	number of cells		Computation duration(hr)
			$x_1$	$x_2$	
1	0.0008	0.0008	2013	750	2.74
2	0.001	0.001	1610	600	1.12
3	0.0012	0.0012	1342	500	0.51
4	0.0014	0.0014	1150	429	0.29

the left, and the gate is 600mm away from the upstream wall of the tank, as shown in Fig.1. The initial dam height is  $H = 300mm$ . The gate opens at  $t' = 0$ , and bore propagates toward downstream. Five pressure sensors are placed at the downstream wall to record the bore pressure. The locations of the sensors,  $S_1$ - $S_5$ , are shown in Fig. 2. More details about the experiment is given in the following sections.

For the RANS computations, two Intel®Xeon E5-2697A v4 processor (16 cores, 40 M Cache, 3.00GHz) are used. Maximum Courant Number is 0.25 and average Courant Number is 0.0086. Four uniform grids are considered in this part which are summarized in Table 2. The RANS model for the grid convergence study is performed in two dimensions only.  $k - \omega$  model is used for the grid convergence study.

Pressure on the downstream wall are recorded in five pressure sensors for these grids. Comparisons of pressure time series on the downstream wall of the four grids are shown in Fig. 3.

Shown in Fig 3, results of Grids 1, 2 and 3 are in good agreement with each other. In Fig. 3 (a), the peak pressures provided by Grids 1, 2 and 3 are higher than the experimental data and that of Grid 4 is lower than the experimental data. These results show that finer grids provide slightly higher pressure peak. This is mainly due to the sensitivity of the peak pressure to specialised time discretization, and the numerical setup. The bore's propagation speed (or arrival time at the downstream wall), when pressure was recorded by Sensor 1 reaches its peak, and its error is compared with experimental data are presented in Table 3. Also given in Table 3 is the peak pressure at Sensor 1 of the different grid configurations, and the associated error when compared with laboratory measurements.

In Table 3, the peak pressure error of Grid 3 is the smallest. The error of propagation speed of Grid 3 is acceptable. We determine that Grid 3 ( $\Delta x_1/h = \Delta x_2/h = 0.0012$ ) can be used in this problem as the peak pressure given by Grid 3 is closer to the experimental data than that of Grids 1 and 2. The grids used by all models for the problems studied here are listed in Table 4.

Next, we shall determine the appropriate turbulence model for the RANS computations of this problem. We consider three turbulence models, namely the  $k - \omega$ ,  $k - \epsilon$  and laminar model. All boundary condition remain the same be-

tween the models. The mesh configuration Grid 3 is used in all turbulence models. The CPU computational time of these turbulence models are 46.67min for the  $k - \omega$ , 46.02min for the  $k - \epsilon$  and 43.67min for the laminar models, all solved in 2D.

Same case as that of [29], shown in Fig. 1, is used for this comparison. The upstream, downstream and bottom walls are set to no-slip boundary conditions in both 2D and 3D studies. The upstream and downstream walls are set with the no-slip boundary conditions in the 3D studies and slip boundary conditions for the 2D studies. Grid 3,  $\Delta x_1/h = \Delta x_2/h = 0.0012$  is chose for the 2D and 3D RANS models here.

Figure 4 shows the comparison of results of the surface elevation studied by use of the laminar,  $k - \omega$  and  $k - \epsilon$  models. Results of the laminar and the  $k - \omega$  models are in close agreement with the experimental data, while the bore predicted by the  $k - \epsilon$  model propagates slower and arrives to the wall about 0.2s later. The differences of the bore speed of these three models are due to the solution of the eddy viscosity terms of each model. Aside from the time difference, results of the laminar and turbulence models are in good agreement with the laboratory measurements for the peak pressure recorded at the sensors. Exception is in sensor  $S_1$ , where  $k - \epsilon$  model has slightly underestimated the peak pressure. This difference is smaller in other sensors.

From these results, we determine that the  $k - \omega$  turbulence model (which shows more sensitivity and closer agreement to laboratory experiment than the laminar model) is appropriate for the cases studied here. This is in agreement with the finding of [42].

## 5 Results and Discussion

Bores generated by breaking of a dam and initial mound of water are studied here. The fundamental difference between these cases is the downstream water depth; in the dam break problem, down stream is either dry or the water depth is much smaller than the initial mound of water. We first consider the dam break case and the experiments carried out by [29]. The RANS and SV equations are used to study the dam break problem. This is followed by discussion of the initial mound of water problem, where downstream water depth is larger than the initial height of the reservoir (above the SWL). The RANS, GN and SV equations are used for the initial mound of water cases.

### Bore Generated by Dam Break

Simulations of the three dimensional experiment of [29] is first presented. The tank used in the experiment is shown in Fig.1. The initial dam height is  $H = 300mm$ . There are five pressure sensors at the downstream wall. The locations of the sensors,  $S_1$ - $S_5$ , are shown in Fig. 2, and discussed in the Section 4.

Shown in Fig. 2, sensor  $S_3$  is used to study the three dimensionality effect. All results are presented in dimensionless form. The experimental data of [29] are given in

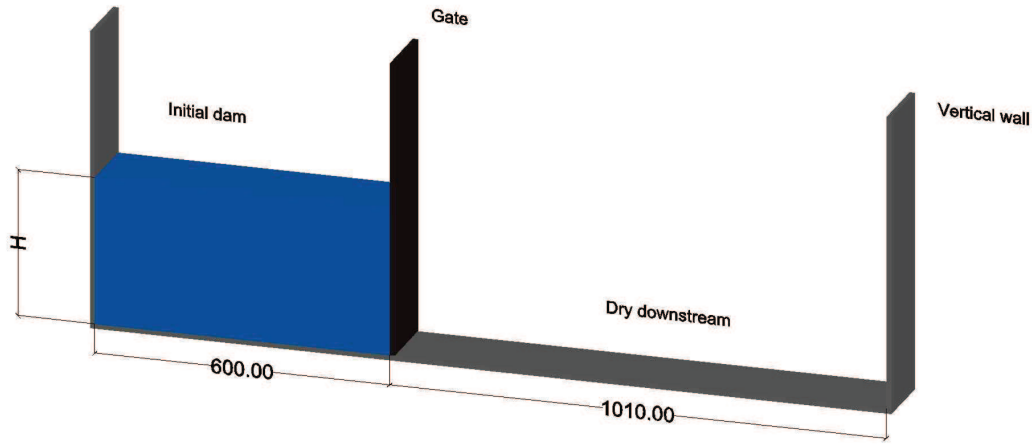


Fig. 1: Schematic of the dam-break experimental tank of [29] used for the comparison purposes. The unit is in mm.

Table 3: Error of propagation speed and peak pressure of different grid configurations when compared to the laboratory experiments of [29].

Grid ID	1	2	3	4	Lab. Experiments
Bore arrival time ( $t'$ )	2.4215	2.4209	2.4238	2.4288	2.457
Error	1.44%	1.47%	1.35%	1.14%	
Peak pressure ( $p'$ )	4.6642	4.2909	3.1971	2.8747	3.0517
Error	52.84%	40.62%	4.76%	5.80%	

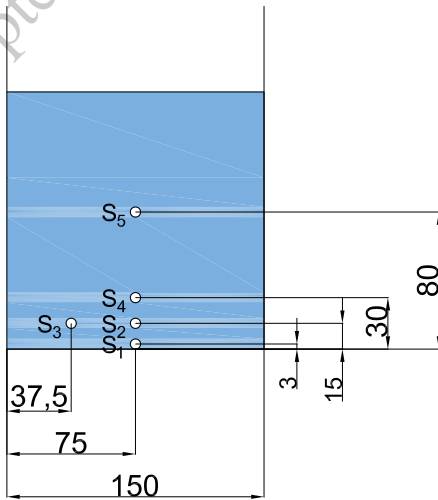


Fig. 2: A front view of the impact wall downstream the tank showing the location of pressure sensors. The unit is in mm.

dimensionless quantities with respect to the constant initial dam height ( $H$ ), water density ( $\rho$ ), and the gravitational acceleration ( $g$ ).

The RANS computations are carried out in both 2D and 3D, for comparison purposes. The grid size in  $x_1$  and  $x_2$  directions of the 3D computations, used for the 3D RANS

Table 4: Grid size of the cases studied in this work. N/A stands for not applicable.

Model	$\Delta x_1/h$	$\Delta x_2/h$
RANS	0.0012	0.0012
GN	0.03	N/A
SV	0.001	N/A

equations, are the same with that of the 2D RANS equations, see Table 2. The grid size in  $x_3$  (into the page) is  $\Delta x_3/h = 0.0012$  and the number of cells in  $x_3$  direction is 125. The 3D RANS computations were completed in about 478 hours, while the 2D RANS computations only cost about 14 hours.

Snapshots of the bore propagations, determined by the 3D RANS equations, are presented in Fig. 5 for 10 times: Figs. 5 (a)-(e) show the bore propagating before impinging at the downstream wall, and Figs. 5 (f)-(j) show the bore evolution along the downstream wall.

In Fig. 6, snapshots of pressure and velocity field of the dam-break bore at (a)  $t' = 2.29$ , (b)  $t' = 2.63$ , (c)  $t' = 2.86$  are shown. The bore arrives at the downstream wall at  $t' = 2.29$ , pressure is zero and the velocity field of bore is mainly horizontal, shown in Figs. 6 (a) and (d).

In Figs. 6 (b) and (e), the bore has arrived at the wall and runs up along the wall at  $t' = 2.63$ . The bore changes

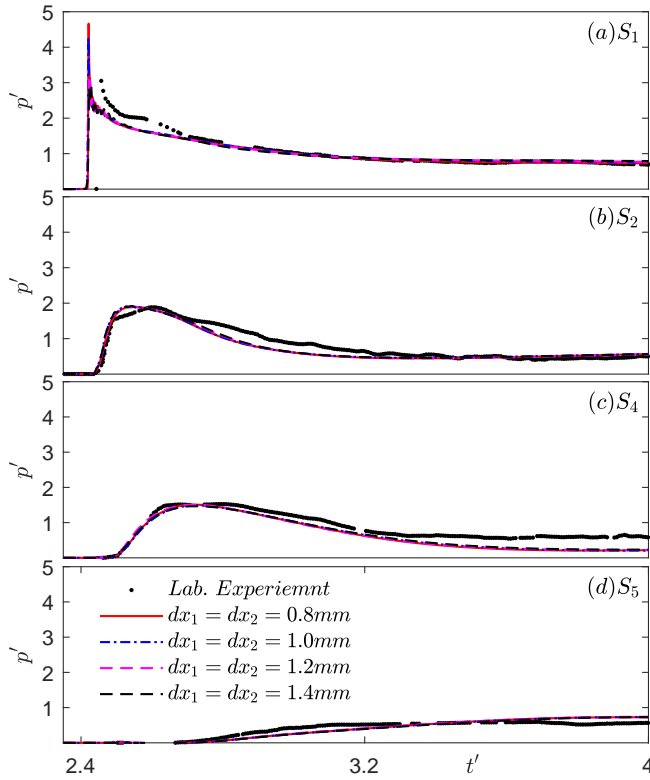


Fig. 3: The grid convergence study of the RANS equations: comparisons of pressure recorded by Sensors  $S_1$ ,  $S_2$ ,  $S_4$  and  $S_5$  computed by the RANS equations vs laboratory measurements of [29].

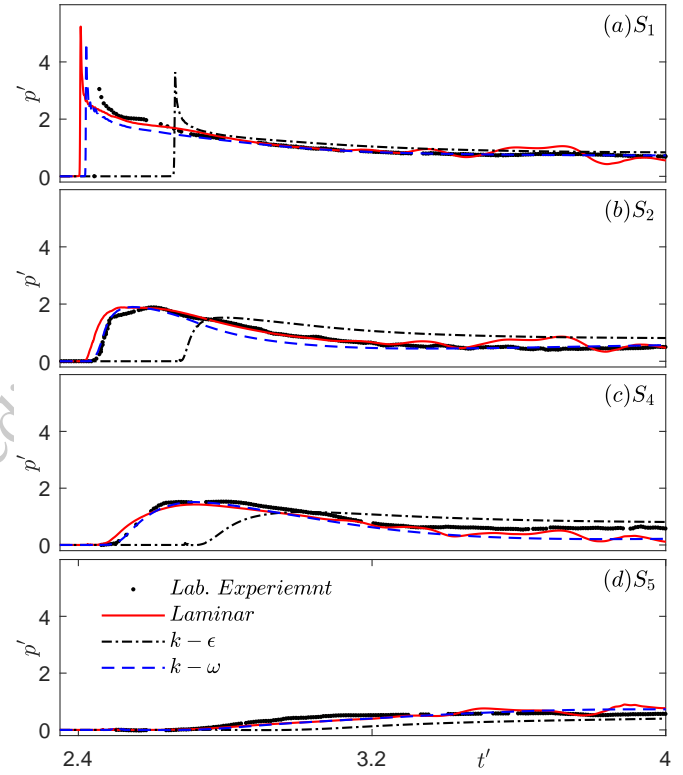


Fig. 4: Comparisons of pressure recorded by Sensors  $S_1$ ,  $S_2$ ,  $S_4$  and  $S_5$  computed by the RANS equations with the laminar model,  $k - \epsilon$  model and  $k - \omega$  model, respectively, vs laboratory measurements of [29].

its velocity direction from horizontal to vertical at the foot of the downstream wall. The flow field is complex at this time. Air bubbles are formed and an area with  $p' = 0$  is found around the foot of the downstream wall. In Figs. 6 (c) and (f), the bore almost reaches the highest point at  $t' = 2.86$ . The velocity vectors of some part of the bore along the downstream wall point backward towards upstream. A negative (gauge) pressure area is found, forming cavitation at that area.

The pressure on the downstream wall computed by the 3D RANS equations, the 2D RANS equations and SV equations are compared with the experimental data in Fig. 7.

Figure 7(a) shows the pressure at Sensor  $S_1$  has a sudden jump to the highest value when the bore arrives at the downstream wall and decreases gradually after that. Good agreement is observed between the 2D and the 3D RANS equations and the experimental data. The pressure at Sensor  $S_1$  computed by the SV equations jumps to the highest value when the bore arrives at the downstream wall, and drops to a small value and increases slowly with fluctuations before  $t' = 3.0$ . The bore speed determined by the SV equations is smaller than others, and the maximum pressure magnitude is underestimated. The difference of the results between the SV equations and others is due to the assumptions made in deriving the SV equations. The bore propagation along the downstream wall, is underestimated by the SV equations, so the pressure computed by the SV equations drop to a small

value.

The bore, computed by 2D and the 3D RANS equations, reach Sensor  $S_1$  at  $t' = 2.415$  and  $t' = 2.421$ , respectively, and at  $t' = 2.592$  by the SV equations and at  $t' = 2.445$  for the experiments. The slight difference between the 2D RANS equations and 3D RANS equations in bore propagation speed is due to the effect of the front and back walls of the tank in the 3D RANS equations. The SV equations have underestimated the bore propagation speed and pressure, due to the assumptions made.

Figures 7(b) and 7(c) show the pressures of Sensors  $S_2$  and  $S_4$ , respectively. At Sensors  $S_2$  and  $S_4$ , pressure of the laboratory experiments and the pressure computed by the 2D RANS equations and 3D RANS equations increases to highest value then decreases gently, while the pressure computed by the SV equations increases with large fluctuations before and at a later time  $t' = 3.0$ .

There is little difference between the pressure of the 2D RANS equations and 3D RANS equations before  $t' = 3.0$ . After that time, some differences can be seen in Figs. 7(b) and 7(c). In the snapshots shown in Fig. 5(i), taken at  $t' = 2.86$ , the bore almost reaches the highest level on the wall and is going to returns towards upstream. Larger differences are seen between the pressure of the 2D RANS equations and 3D RANS equations at this point, as the resistance from the upstream and downstream walls on the bore is significant. Hence, it appears that the 2D RANS equations model can be

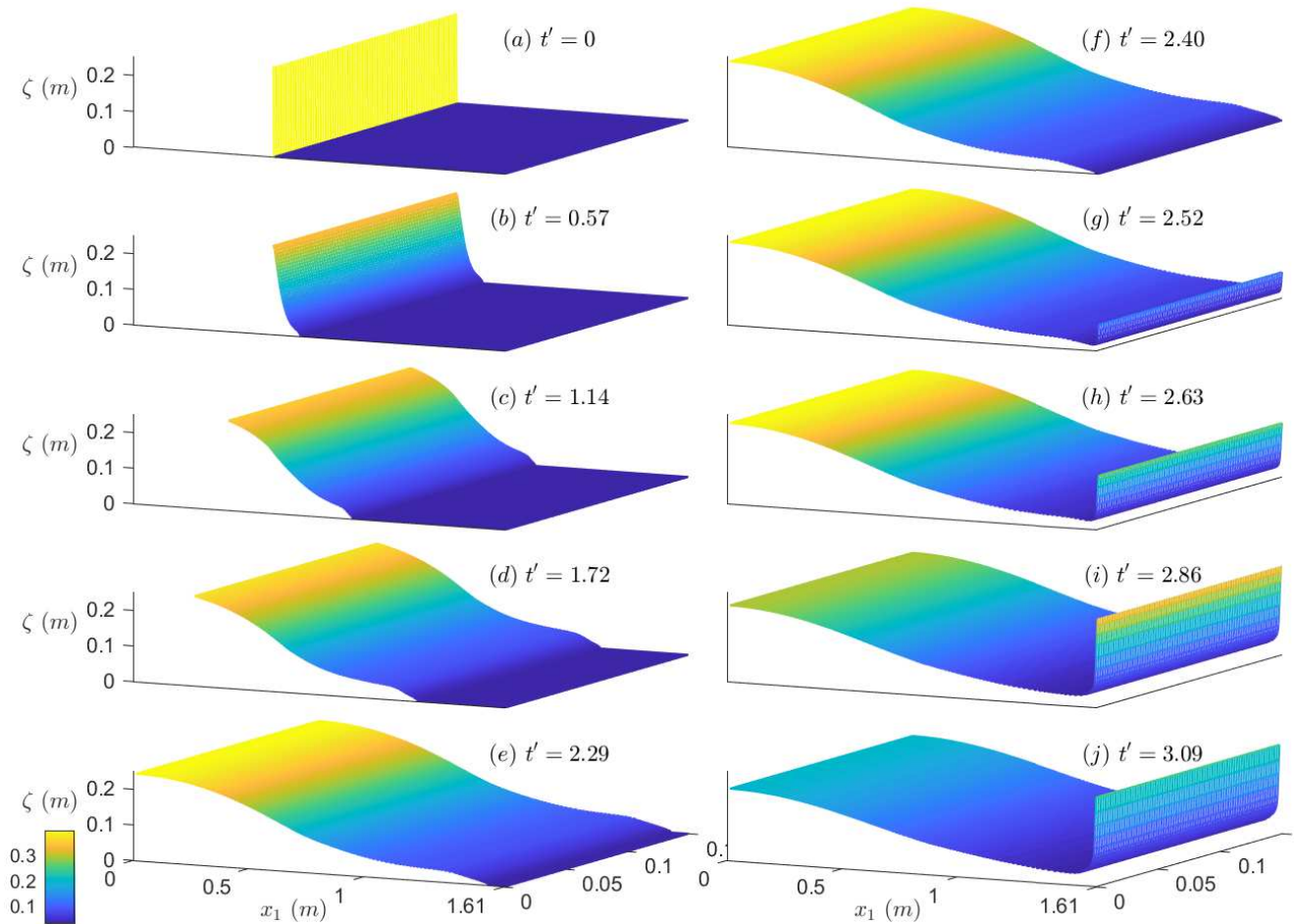


Fig. 5: Snapshots of the dam-break bore at (a)  $t' = 0$ , (b)  $t' = 0.57$ , (c)  $t' = 1.14$ , (d)  $t' = 1.72$ , (e)  $t' = 2.29$ , (f)  $t' = 2.40$ , (g)  $t' = 2.52$ , (h)  $t' = 2.63$ , (i)  $t' = 2.86$  and (j)  $t' = 3.09$ .

safely used to study the pressure on downstream wall before the bore reaches the highest level.

Figure 7(d) shows the pressure at Sensor  $S_5$ . At this sensor, the pressure of the experiments and the pressure computed by the 2D RANS equations and 3D RANS equations increase gently without experiencing a peak. This is because the horizontal bore speed is smaller at the position of Sensor  $S_5$ , when compared to the other sensors. The pressure computed by the SV equations increase with fluctuations.

At  $t' = 4$ , the pressure given by the RANS equation agree well with the experimental data at Sensor  $S_1$ , while slight difference is observed at Sensor  $S_2$  and the difference increases at Sensor  $S_4$ . The differences between results of different models at Sensor  $S_1$ ,  $S_2$  and  $S_4$  is likely due to the formation of air bubble and partially surface tension. In experiments, the breaking of air bubbles formed in the bore should result in larger pressure on the wall.

To study the three dimensionality effect on the bore pressure, recordings of sensors  $S_2$  and  $S_3$  are compared with each other and shown in Fig. 8. In this figure, results of the 2D and 3D RANS equations are also included. The results of 3D RANS equations at  $S_2$  on top of Sensor  $S_3$ .

Shown in Fig. 8, the 2D and 3D RANS results agree

well with the experiments on that there is little to no difference of the peak pressure of sensors  $S_2$  and  $S_3$ , *i.e.* there is no 3D effect on the peak pressure. The computational models, however, seem to predict very slightly faster bore peaks.

Some small differences between the computational models and laboratory experiments are observed in the pressure after the peak, where the models have slightly underestimated the pressure. The underestimation should be due to the surface tension effects as the water leaves the wall, and formation of the air bubbles and wall friction. Again, there is little to no difference between the 2D and 3D models, revealing that the three dimensionality does not play any noticeable role in this problem.

Overall, the pressures on the downstream wall computed by the 2D RANS equations and 3D RANS equations agree well with the pressure peak measured by the five sensors in the laboratory experiment of [29].

### Bore Generated by Initial Mound of Water

In this section, we study the bore generation, propagation and pressure due to an initial mound of water. The significant difference of this case, when compared to the dam-break problem, is due to the downstream water depth. Com-

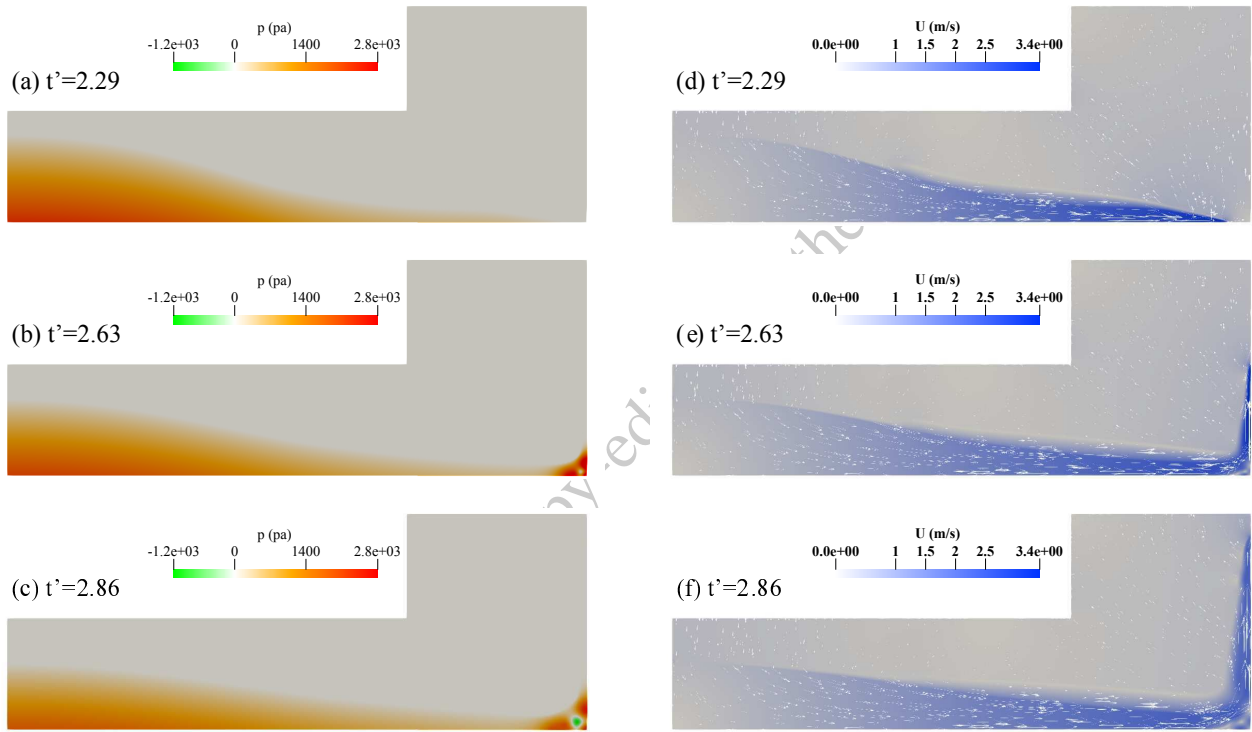


Fig. 6: The snapshots of pressure and velocity field of the dam-break bore at different times.

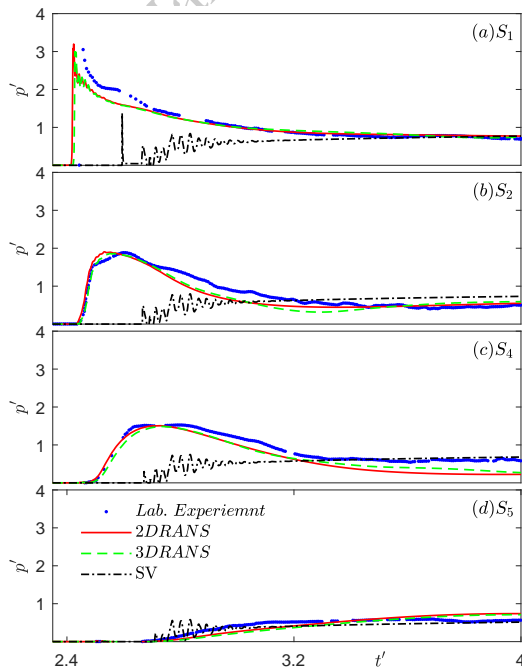


Fig. 7: Comparisons of bore pressure time series of laboratory measurements of [29], the 2D RANS equations, 3D RANS equations and SV equations at Sensors (a) $S_1$ , (b) $S_2$  (c) $S_4$  and (d) $S_5$ .

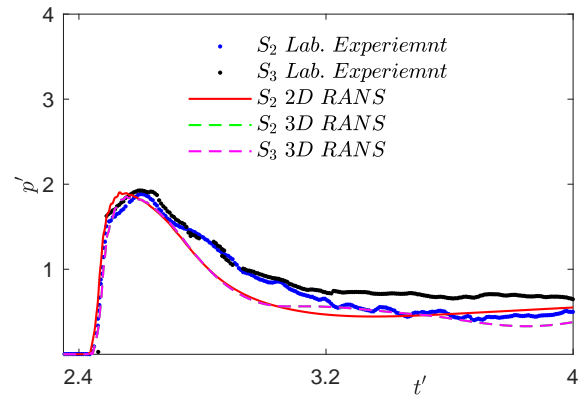


Fig. 8: Comparisons of bore pressure time series of laboratory measurements of [29], the 2D RANS equations and 3D RANS equations at Sensors  $S_2$  and  $S_3$ .

where  $A$  is the water amplitude (above the SWL) at the reservoir. The RANS, GN and SV models are used in this section. Results of the GN equations have been validated by many others for various hydrodynamic problems, see *e.g.* [30,70,71], where excellent agreement between results of the GN equations and laboratory experiments for soliton fission and loads are observed. The length of the computational domain is defined such that the computations stop before waves arrive at the downstream boundary.

At time  $t' = 0$ , water is at rest. After that, gate at  $x_1 = L$  is removed instantly and completely. Several solitons are generated and move towards downstream without significant

putations of this section is in two dimensions.

A schematic of the numerical tank is shown in Fig. 9. Note that in the case of an initial mound of water,  $A < h$ ,

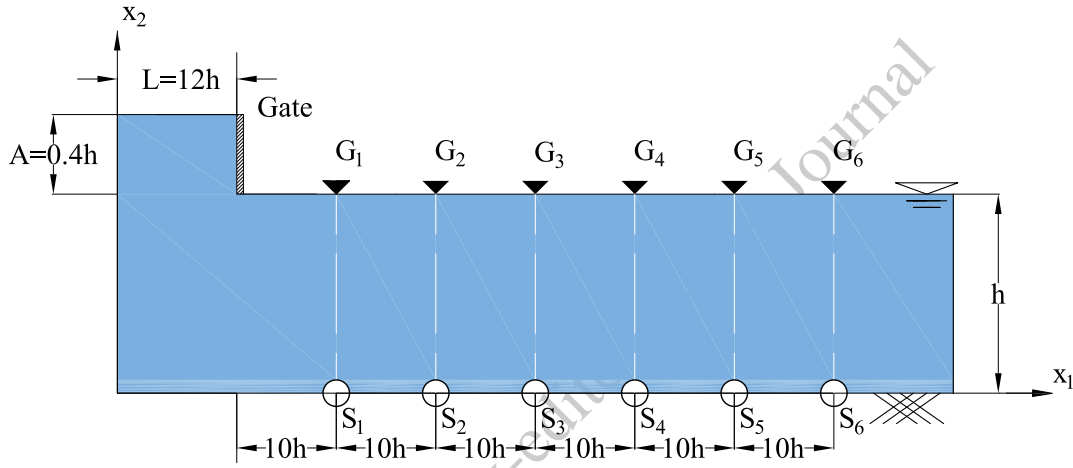


Fig. 9: Schematic of the numerical tank of the initial mound of water problem and location of the wave gauges and the pressure sensors. Figure not to scale.

change in wave amplitude, details can be seen in *e.g.* [30]. We consider a case with initial mound amplitude  $A = 0.4h$ , and initial length  $L = 12h$ . Six pressure sensors and six wave gauges are located on the tank floor to measure the pressure on the base. Locations of the gauges and sensors are shown in Fig. 9.

The GN computations are carried out for dimensionless variables with respect to the downstream water depth. The downstream water depth  $h = 1m$  is constant in the RANS and the SV computations.

Snapshots of the surface elevation computed by the RANS equations, the GN equations and the SV equations at  $t' = 30, 50, 70$  are shown in Fig. 10. The vertical axis shows the surface elevation of water. The results of the computational models are in close agreement for the leading solitons, but the results of the SV equations lose the details and has only provided the average.

The pressures on the tank floor computed by the RANS equations and the SV equations are compared with that of the GN equations in Fig. 11. The bore pressure is recorded by six sensors on the tank floor shown in Fig. 9. Also shown in Fig. 9 is the wave gauges, located exactly above the pressure sensors, used to measure the surface elevation.

In Fig. 11, the left column shows the surface elevation, and the right column is the bottom pressure at the same locations. Figures 11(a) and 11(g) show the surface elevations of gauge  $G_1$  and the pressure at Sensor  $S_1$ , respectively, computed by the GN equations, RANS equations and SV equations. Overall, results of the RANS and GN equations are in close agreement, while the SV equations have simplified the solution. The surface elevation and pressure computed by the GN equations show larger fluctuations than the results of the RANS equations. This is due to the numerical fluctuation found near the gate of the GN model, see Fig.10.

Figures 11(b)-11(f) and 11(h)-11(l) show the surface elevations of Gauges  $G_2 - G_6$  and pressures of Sensors  $S_2 - S_6$ , respectively, computed by the GN equations, RANS equations and SV equations. Results are in good agreements, ex-

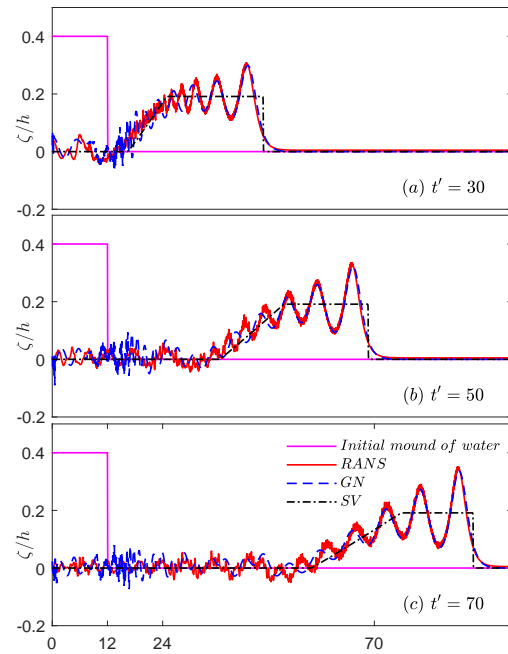


Fig. 10: Snapshots of the computational model at different times. ( $A = 0.4h, L = 12h$ ).

cept for the SV equation, which mainly show average value. The results of the GN equations do not show the fluctuations any more for the gauges and sensors are far from the gate.

In Fig. 12, the total pressure and hydrostatic pressure at Sensor  $S_6$  is compared for the (a) RANS, (b) GN and (c) SV equations, respectively. The mean value of total pressure agree well with that of hydrostatic pressure for these three equations, revealing that hydrodynamic pressure is dominant in these cases. Figure 12 (c) shows that the SV equations cannot provide the hydrodynamic pressure as it only considers hydrostatic pressure.

Overall, the surface elevation and pressure computed by the GN equations show good agreement with results of the

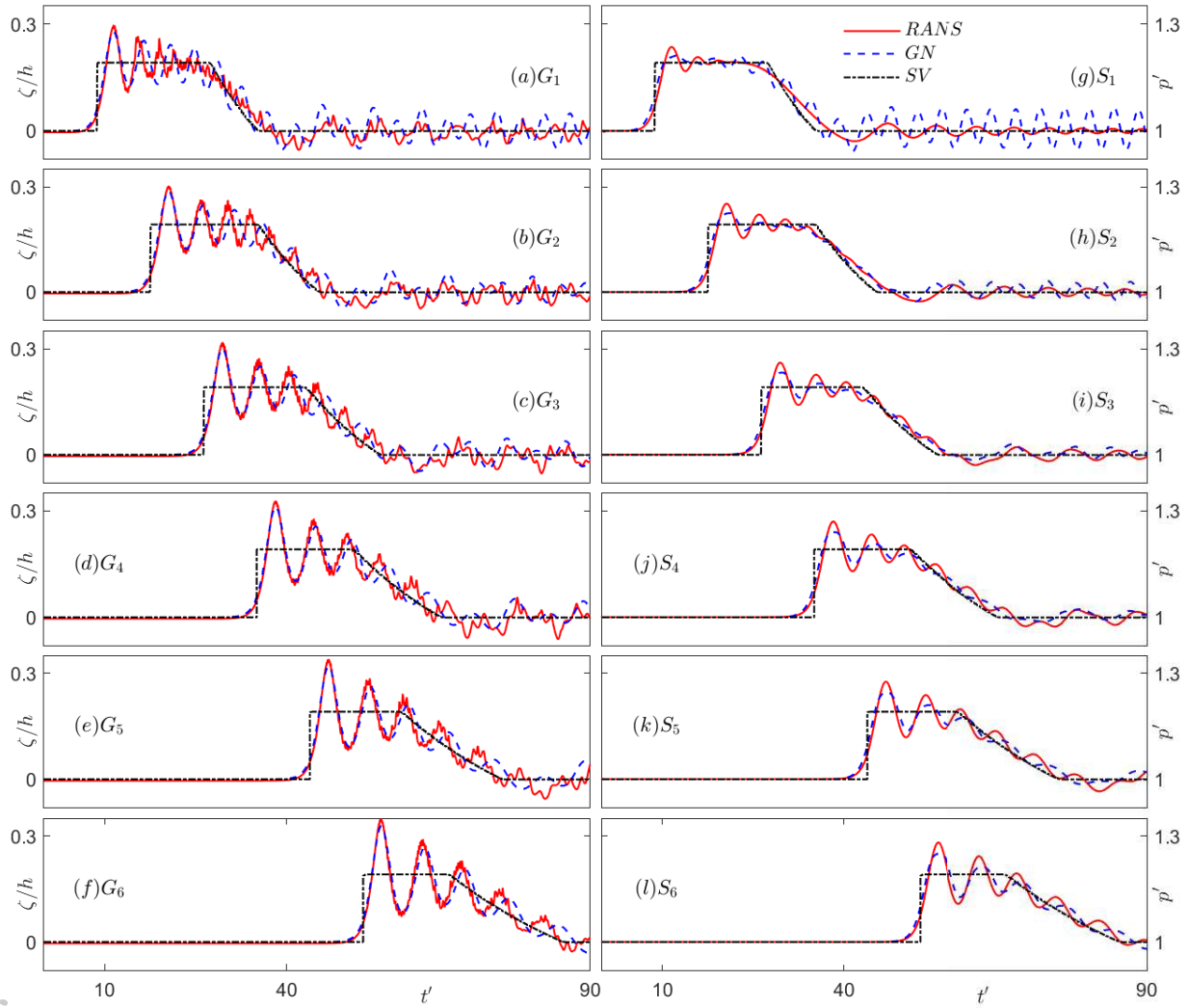


Fig. 11: Comparison of the results of RANS, GN and SV equations for surface elevations of an initial mound of water at Gauges (a) $G_1$ , (b) $G_2$ , (c) $G_3$ , (d) $G_4$ , (e) $G_5$  and (f) $G_6$  and pressures at Sensors (g) $S_1$ , (h) $S_2$ , (i) $S_3$ , (j) $S_4$ , (k) $S_5$  and (l) $S_6$  ( $A = 0.4h$ ,  $L = 12h$ ).

RANS equations, while the SV equations only provide average information. The SV equations and GN equations appear to show less sensitivity to the pressure than the RANS equations. The bottom pressure shows close relation with the free-surface fluctuations. Hence hydrostatic pressure is the main component of the bottom pressure in the initial mound of water problem.

## 6 Concluding Remarks

The 2D RANS equations, the 3D RANS equations and the SV equations are used to study the dam-break problem, where initial height of the water is much larger than the downstream water depth. The pressure on the downstream wall of these three models are compared with laboratory experiments.

To study the effect of viscosity, laminar,  $k - \epsilon$  and  $k - \omega$  models are used. The bore propagation speed of these three models are slightly different because of the differences in

the solution of the eddy viscosity terms in each model. It is found that the  $k - \omega$  model provides better agreement with the laboratory measurements of the dam break problem.

Pressures computed by the 2D RANS equations and 3D RANS equations agree well with each other before the bore reaches the highest point on the downstream wall. Some slight difference are observed, mainly due to the effect of the front and back walls, and the possibility of the flow into the page in the 3D model. As the 3D model is computationally more costly, 2D model is suggested when the interest is confined to the pressure before bore approaches the highest point on the downstream wall.

Pressure computed by the SV equations agrees well with the RANS equations and experimental data when the pressure sensor is high enough on the wall, as in Sensor  $S_5$ . But the SV equations underestimate the bore height and speed and hence shows less sensitivity with the sudden change of water height. In the SV equations, pressure distribution is

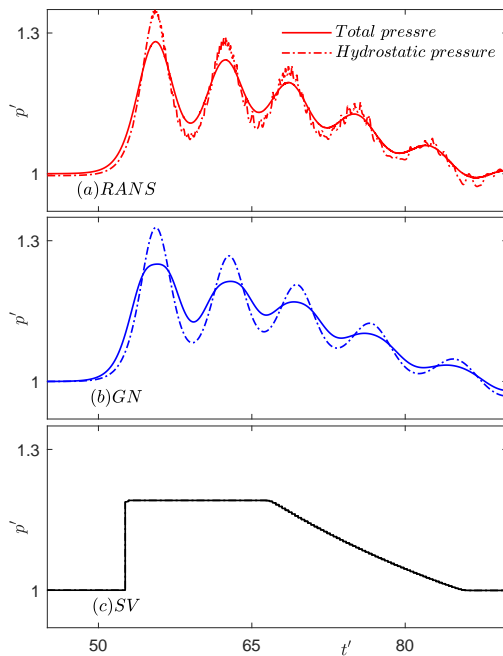


Fig. 12: Comparison of the total pressure with the hydrostatic pressure of initial mound of water of the (a) RANS, (b) GN and (c) SV equations at Sensor  $S_6$  ( $A = 0.4h$ ,  $L = 12h$ ).

simplified by hydrostatic distribution and the momentum direction is restricted to one dimension.

The pressure peaks computed by 2D and the 3D RANS equations agree well with the experimental data, although there are slight differences in the time of the pressure peak. The maximum pressure results provided by the RANS equations seems to be acceptable for engineering applications.

The RANS equations, GN equations and SV equations are used to study the generation, propagation and pressure of an initial mound of water. The equations show close agreement for the generation and propagation of bore of initial mound of water. The results of the SV equations has significantly lost the details.

Overall, close agreement is observed between the results of the RANS equations, GN equations. In the GN equations, the function  $\zeta$  (surface elevation) is single-valued. Hence, application of the GN equations is limited to cases that do not involve wave breaking or dry seabed. Given that the computational cost of the GN equations (often less than a minute) is much less than that of the RANS equations, the GN equations appear to be a good substitute to the RANS equations in these cases.

## References

- [1] Chanson, H., 2006. "Tsunami surges on dry coastal plains: Application of dam break wave equations". *Coastal engineering journal*, **48**(04), pp. 355–370.
- [2] Cross, R. H., 1967. "Tsunami surge forces". *Journal of the waterways and harbors division*, **93**(4), pp. 201–231.
- [3] Yeh, H., 2006. "Maximum fluid forces in the tsunami runup zone". *Journal of waterway, port, coastal, and ocean engineering*, **132**(6), pp. 496–500.
- [4] Kihara, N., Niida, Y., Takabatake, D., Kaida, H., Shibayama, A., and Miyagawa, Y., 2015. "Large-scale experiments on tsunami-induced pressure on a vertical tide wall". *Coastal Engineering*, **99**, pp. 46–63.
- [5] Linton, D., Gupta, R., Cox, D., van de Lindt, J., Oshnack, M. E., and Clauson, M., 2012. "Evaluation of tsunami loads on wood-frame walls at full scale". *Journal of Structural Engineering*, **139**(8), pp. 1318–1325.
- [6] Mizutani, S., and Imamura, F., 2001. "Dynamic wave force of tsunamis acting on a structure". In Proc. of the International Tsunami Symposium, pp. 7–28.
- [7] Robertson, I. N., Paczkowski, K., Riggs, H., and Mohamed, A., 2011. "Tsunami bore forces on walls". In ASME 2011 30th International Conference on Ocean, Offshore and Arctic Engineering, Rotterdam, The Netherlands, American Society of Mechanical Engineers, pp. 395–403.
- [8] Robertson, I. N., Carden, L. P., and Chock, G. Y., 2013. "Case study of tsunami bore impact on RC wall". In ASME 2013 32nd International Conference on Ocean, Offshore and Arctic Engineering, American Society of Mechanical Engineers, pp. V005T06A077–V005T06A085.
- [9] Santo, J., and Robertson, I. N., 2010. "Lateral loading on vertical structural elements due to a tsunami bore". *University of Hawaii, Honolulu, Report No. UHM/CEE/10-02*, pp. 107–137.
- [10] Rahman, S., Akib, S., Khan, M., and Shirazi, S., 2014. "Experimental study on tsunami risk reduction on coastal building fronted by sea wall". *The Scientific World Journal*, **2014**, pp. 94–101, DOI:10.1155/2014/729357.
- [11] Thusyanthan, N. I., and Gopal Madabhushi, S., 2008. "Tsunami wave loading on coastal houses: a model approach". In Proceedings of the institution of civil engineers-civil engineering, Vol. 161, Thomas Telford Ltd, pp. 77–86.
- [12] Wijatmiko, I., and Murakami, K., 2012. "Hydrodynamics: Theory and model". BoD–Books on Demand, ch. 3, pp. 59–78.
- [13] Asakura, R., 2000. "An experimental study on wave force acting on on-shore structures due to overflowing tsunamis". In Proceedings of Coastal Engineering, JSCE. Tokyo and Yokohama, Japan, Vol. 47, pp. 911–915.
- [14] Chinnarasri, C., Thanasisathit, N., Ruangrassamee, A., Weesakul, S., and Lukkunaprasit, P., 2013. "The impact of tsunami-induced bores on buildings". In Proceedings of the institution of civil engineers-maritime engineering, Vol. 166, Thomas Telford Ltd, pp. 14–24.
- [15] Fujima, K., Achmad, F., Shigihara, Y., and Mizutani, N., 2009. "Estimation of tsunami force acting on rectangular structures". *Journal of Disaster Research*, **4**(6), pp. 404–409.
- [16] Nouri, Y., Nistor, I., Palermo, D., and Cornett, A.,

2010. "Experimental investigation of tsunami impact on free standing structures". *Coastal Engineering Journal*, **52**(01), pp. 43–70.
- [17] Palermo, D., Nistor, I., Al-Faesly, T., and Cornett, A., 2012. "Impact of tsunami forces on structures: The university of ottawa experience". In Proceedings of the fifth international tsunami symposium, Ispra, Italy, pp. 3–5.
- [18] Palermo, D., Nistor, I., Nouri, Y., and Cornett, A., 2009. "Tsunami loading of near-shoreline structures: a primer". *Canadian Journal of Civil Engineering*, **36**(11), pp. 1804–1815.
- [19] Robertson, I., Riggs, H., and Mohamed, A., 2008. "Experimental results of tsunami bore forces on structures". In 27th Int. Conf. Offshore Mechanics and Arctic Engineering, Estoril, Portugal, USA, Vol. 135, pp. 585–601.
- [20] Pilotti, M., Maranzoni, A., Tomirotti, M., and Valerio, G., 2010. "1923 Gleno dam break: Case study and numerical modeling". *Journal of Hydraulic Engineering*, **137**(4), pp. 480–492.
- [21] Seed, H. B., and Duncan, J. M., 1981. "The teton dam failure—a retrospective review". In Soil mechanics and foundation engineering: proceedings of the 10th international conference on soil mechanics and foundation engineering, Stockholm, Sweden, pp. 15–19.
- [22] Yalciner, A. C., Perincek, D., Ersoy, S., Presateya, G., Hidayat, R., and McAdoo, B., 2005. "Report on December 26, 2004, Indian Ocean Tsunami, Field Survey on Jan 21–31 at North of Sumatra". In Proceedings of the 14th Symposium Naval Hydrodynamics. Washington, U.S.A., GEOLOGICAL SURVEY OF CANADA (GSC), pp. 53–73.
- [23] West, M., Sánchez, J. J., and McNutt, S. R., 2005. "Periodically triggered seismicity at Mount Wrangell, Alaska, after the Sumatra earthquake". *Science*, **308**(5725), pp. 1144–1146.
- [24] Ritter, A., 1892. "Die fortpflanzung der wasserwellen". *Zeitschrift des Vereines Deutscher Ingenieure*, **36**(33), pp. 947–954.
- [25] Hu, C., and Kashiwagi, M., 2004. "A CIP-based method for numerical simulations of violent free-surface flows". *Journal of Marine Science and Technology*, **9**(4), pp. 143–157.
- [26] Zhou, Z., De Kat, J., and Buchner, B., 1999. "A nonlinear 3d approach to simulate green water dynamics on deck". In Proceedings of the Seventh International Conference on Numerical Ship Hydrodynamics, Nantes, France, pp. 1–15.
- [27] Kleefsman, K., Fekken, G., Veldman, A., Iwanowski, B., and Buchner, B., 2005. "A volume-of-fluid based simulation method for wave impact problems". *Journal of Computational Physics*, **206**(1), pp. 363–393.
- [28] Wemmenhove, R., Gladsø, R., Iwanowski, B., and Lefranc, M., 2010. "Comparison of CFD calculations and experiment for the dambreak experiment with one flexible wall". In The Twentieth International Offshore and Polar Engineering Conference, Beijing, China, International Society of Offshore and Polar Engineers.
- [29] Lobovský, L., Botia-Vera, E., Castellana, F., Mas-Soler, J., and Souto-Iglesias, A., 2014. "Experimental investigation of dynamic pressure loads during dam break". *Journal of Fluids and Structures*, **48**, pp. 407–434.
- [30] Ertekin, R. C., Hayatdavoodi, M., and Kim, J. W., 2014. "On some solitary and cnoidal wave diffraction solutions of the Green-Naghdi equations". *Applied Ocean Research*, **47**, pp. 125–137, DOI: 10.1016/j.apor.2014.04.005.
- [31] Robison, J., and Scott Russell, J., 1837. "Report of the committee on waves". In 7th Meeting of the British Association for the Advancement of Science, Liverpool, UK, p. 226.
- [32] Lighthill, M. J., and Lighthill, J., 1978. *Waves in fluids*. Cambridge university press.
- [33] Stoker, J. J., 1957. *Water waves: The mathematical theory with applications*, Vol. 36. John Wiley & Sons.
- [34] Johnson, R. S., 1997. *A modern introduction to the mathematical theory of water waves*, Vol. 19. Cambridge university press.
- [35] Craig, W., 2002. "Non-existence of solitary water waves in three dimensions". *Philosophical Transactions of the Royal Society of London. Series A: Mathematical, Physical and Engineering Sciences*, **360**(1799), pp. 2127–2135.
- [36] Evans, W., and Ford, M., 1996. "An exact integral equation for solitary waves (with new numerical results for some 'internal' properties)". *Proceedings of the Royal Society of London. Series A: Mathematical, Physical and Engineering Sciences*, **452**(1945), pp. 373–390.
- [37] Tsai, C.-H., Huang, M.-C., Young, F.-J., Lin, Y.-C., and Li, H.-W., 2005. "On the recovery of surface wave by pressure transfer function". *Ocean Engineering*, **32**(10), pp. 1247–1259.
- [38] Escher, J., and Schlurmann, T., 2008. "On the recovery of the free surface from the pressure within periodic traveling water waves". *Journal of Nonlinear Mathematical Physics*, **15**(sup2), pp. 50–57.
- [39] Constantin, A., Escher, J., and Hsu, H.-C., 2011. "Pressure beneath a solitary water wave: mathematical theory and experiments". *Archive for rational mechanics and analysis*, **201**(1), pp. 251–269.
- [40] Ferziger, J. H., and Peric, M., 2012. *Computational methods for fluid dynamics*, Vol. 3. Springer Science & Business Media.
- [41] Menter, F. R., 1993. "Zonal two equation  $k - \epsilon$  turbulence models for aerodynamic flows". In 23rd Fluid Dynamics, Plasmadynamics, and Lasers Conference, Orlando, Florida, U.S.A., pp. 1–21.
- [42] Menter, F. R., Kuntz, M., and Langtry, R., 2003. "Ten years of industrial experience with the SST turbulence model". *Turbulence, heat and mass transfer*, **4**(1), pp. 625–632.
- [43] Wilcox, D. C., 1998. *Turbulence modeling for CFD*, Vol. 2. DCW industries La Canada, CA.
- [44] Mokrani, C., and Abadie, S., 2016. "Conditions for

- peak pressure stability in vof simulations of dam break flow impact”. *Journal of Fluids and Structures*, **62**, pp. 86–103.
- [45] Hirt, C. W., and Nichols, B. D., 1981. “Volume of fluid (VOF) method for the dynamics of free boundaries”. *Journal of Computational Physics*, **39**(1), pp. 201–225.
- [46] Greenshields, C. J., 2018. “OpenFOAM user guide”. *OpenFOAM Foundation Ltd, version*, 3(1).
- [47] Higuera, P., Lara, J. L., and Losada, I. J., 2013. “Realistic wave generation and active wave absorption for Navier–Stokes models: Application to OpenFOAM®”. *Coastal Engineering*, **71**, pp. 102–118.
- [48] Green, A. E., Laws, N., and Naghdi, P. M., 1974. “On the theory of water waves”. *Proc. R. Soc. Lond. A*, **338**(1612), pp. 43–55.
- [49] Green, A. E., and Naghdi, P. M., 1976. “Directed fluid sheets”. *Proceedings of the Royal Society of London*, **347**(1651), pp. 447–473.
- [50] Green, A. E., and Naghdi, P. M., 1976. “A derivation of equations for wave propagation in water of variable depth”. *Journal of Fluid Mechanics*, **78**(2), pp. 237–246.
- [51] Ertekin, R. C., 1984. “Soliton generation by moving disturbances in shallow water: theory, computation and experiment”. PhD thesis, University of California at Berkeley.
- [52] Hayatdavoodi, M., and Ertekin, R. C., 2015. “Non-linear wave loads on a submerged deck by the green-naghdi equations”. *Journal of Offshore Mechanics and Arctic Engineering*, **137**(1), p. 011102.
- [53] Hayatdavoodi, M., and Ertekin, R. C., 2015. “Wave forces on a submerged horizontal plate. Part I: Theory and modelling”. *Journal of Fluids and Structures*, **54**(April), pp. 566–579.
- [54] Hayatdavoodi, M., and Ertekin, R. C., 2015. “Wave forces on a submerged horizontal plate. Part II: Solitary and cnoidal waves”. *Journal of Fluids and Structures*, **54**(April), pp. 580–596.
- [55] Hayatdavoodi, M., Ertekin, R. C., and Valentine, B. D., 2017. “Solitary and cnoidal wave scattering by a submerged horizontal plate in shallow water”. *AIP Advances*, **7**(6), p. 065212.
- [56] Neill, D. R., Hayatdavoodi, M., and Ertekin, R. C., 2018. “On solitary wave diffraction by multiple, in-line vertical cylinders”. *Nonlinear Dynamics*, **91**(2), pp. 975–994.
- [57] Hayatdavoodi, M., Neill, D. R., and Ertekin, R. C., 2018. “Diffraction of cnoidal waves by vertical cylinders in shallow water”. *Theoretical and Computational Fluid Dynamics*, **32**(5), pp. 561–591.
- [58] Zhao, B. B., Duan, W. Y., and Ertekin, R. C., 2014. “Application of higher-level GN theory to some wave transformation problems”. *Coastal Engineering*, **83**, 1, pp. 177–189, DOI:10.1016/j.coastaleng.2013.10.010.
- [59] Zhao, B. B., Ertekin, R. C., Duan, W. Y., and Hayatdavoodi, M., 2014. “On the steady solitary-wave solution of the Green–Naghdi equations of different levels”. *Wave Motion*, **51**(8), pp. 1382–1395, DOI:10.1016/j.wavemoti.2014.08.009.
- [60] Zhao, B. B., Duan, W. Y., Ertekin, R. C., and Hayatdavoodi, M., 2015. “High-level Green–Naghdi wave models for nonlinear wave transformation in three dimensions”. *Journal of Ocean Engineering and Marine Energy*, **1**(2), pp. 121–132, DOI:10.1007/s40722–014–0009–8.
- [61] Saint-Venant, A. d., 1871. “Theorie du mouvement non permanent des eaux, avec application aux crues des rivieres et a l’introduction de marees dans leurs lits”. *Comptes rendus des seances de l’Academie des Sciences*, **36**, pp. 147–237.
- [62] Mises, R. V., 1945. “On Saint Venant’s principle”. *Bulletin of the American Mathematical Society*, **51**(8), pp. 555–562.
- [63] Manning, R., 1889. “On the flow of water in open channels and pipes.”. *Institution of Civil Engineers of Ireland*, **20**, pp. 161–207.
- [64] Kundu, P., and Cohen, L., 1990. *Fluid mechanics*. Academic Press.
- [65] Jameson, A., Schmidt, W., and Turkel, E., 1981. “Numerical solution of the Euler equations by finite volume methods using Runge Kutta time stepping schemes”. In 14th fluid and plasma dynamics conference, Palo Alto, California, U.S.A., p. 1259.
- [66] Issa, R. I., 1986. “Solution of the implicitly discretised fluid flow equations by operator-splitting”. *Journal of Computational Physics*, **62**(1), pp. 40–65.
- [67] Holzmann, T., 2016. “Mathematics, numerics, derivations and openfoam®”. *Loeben, Germany: Holzmann CFD*.
- [68] Ertekin, R. C., Webster, W. C., and Wehausen, J. V., 1986. “Waves caused by a moving disturbance in a shallow channel of finite width”. *Journal of Fluid Mechanics*, **169**, pp. 275–292.
- [69] Morris, A. G., 2013. “Adapting cartesian cut cell methods for flood risk evaluation”. PhD thesis, Manchester Metropolitan University.
- [70] Hayatdavoodi, M., Seiffert, B., and Ertekin, R. C., 2015. “Experiments and calculations of cnoidal wave loads on a flat plate in shallow-water”. *Journal of Ocean Engineering and Marine Energy*, **1**(1), pp. 77–99, DOI: 10.1007/s40722–014–0007–x.
- [71] Hayatdavoodi, M., Treichel, K., and Ertekin, R. C., 2019. “Parametric study of nonlinear wave loads on submerged decks in shallow water”. *Journal of Fluids and Structures*, **86**, pp. 266–289, DOI: 10.1016/j.jfluidstructs.2019.02.016.